Available online at www.sciencedirect.com
ScienceDirect
Physics of the Earth and Planetary Interiors 164 (2007) 50–62
PHYSICS OF THE EARTH AND PLANETARY INTERIORS
www.elsevier.com/locate/pepi

The perovskite to post-perovskite transition in $CaIrO_3$: Clapeyron slope and changes in bulk and shear moduli by density functional theory

Svein Stølen [a,*], Reidar G. Trønnes [b]

[a] *Department of Chemistry and Centre for Materials Science and Nanotechnology, University of Oslo, Postbox 1033 Blindern, N-0315 Oslo, Norway*
[b] *Natural History Museum, Geology, University of Oslo, Postbox 1172 Blindern, N-0318 Oslo, Norway*

Received 6 March 2007; received in revised form 8 May 2007; accepted 24 May 2007

Abstract

The thermodynamic properties of perovskite (pv) and post-perovskite (ppv) of $CaIrO_3$ are derived from total energy calculations using density functional theory. Negative molar volume and enthalpy changes of 0.40 cm^3 mol^{-1} and 11.8 kJ mol^{-1} for the pv to ppv transition at 0 K stabilize ppv at low temperatures and high-pressures. Vibrational entropies calculated in the harmonic approximation, using the direct method, favour pv with increasing temperatures (105.5 J K^{-1} mol^{-1} for pv versus 99.2 J K^{-1} mol^{-1} for ppv at 298 K). A main reason for the lower entropy of post-perovskite compared to perovskite is probably related to constraints on certain vibrational modes imposed by edge-sharing of octahedra in post-perovskite. The Clapeyron slope of the pv–ppv phase boundary is deduced from the calculated enthalpy and volume of transition in conjunction with an experimental transition temperature. The resulting dp/dT of 18 MPa K^{-1} is in good agreement with experimental determinations reported in literature. The high-pressure properties were calculated from the variation of the total energy with volume using the Murnaghan (M) and the Birch–Murnaghan (B–M) equations-of-state. The two methods give the same values for the bulk modulus but somewhat different values for the pressure derivative of the bulk modulus: $K_0 = 178$ GPa and $K_0' = 2.8$ (M) and 3.3 (B–M) for pv compared to $K_0 = 164$ GPa and $K_0' = 3.9$ (M) and 4.0 (B–M) for ppv. By holding K_0' for pv fixed at 4.0, K_0 is reduced to 172 GPa. The bulk moduli at zero pressure were also derived through calculation of the elastic constants giving $K_0 = 172$ GPa for pv compared to $K_0 = 157$ GPa for ppv. In order to compare the changes in the bulk and shear moduli across the pv–ppv phase transition, also the shear moduli were derived from the elastic constants. Whereas the bulk modulus decreases by about 9% from perovskite to post-perovskite, the shear modulus increases by about 15% across the transition. The elastic parameters obtained for the $CaIrO_3$ polymorphs are consistent with those of $MgSiO_3$ and with seismic velocity variations in the lowermost mantle. Our DFT-results demonstrate that $CaIrO_3$ may be a useful low-pressure analogue for studies of the general properties of the pv–ppv-transition relevant to the D″ layer since the negative and positive changes in bulk and shear moduli, respectively, across the pv- to ppv-transition boundary appear to be strongly linked to the nature of the two crystal structures.

Keywords: Perovskite; Post-perovskite; Calcium iridium(IV) oxide; Density functional theory; Thermodynamics; Elastic properties

1. Introduction

The recent discovery of a phase transition from $MgSiO_3$-dominated perovskite (pv) (space group *Pbnm*) to a post-perovskite (ppv) phase with $CaIrO_3$-type struc-

* Corresponding author.
E-mail address: svein.stolen@kjemi.uio.no (S. Stølen).

0031-9201/$ – see front matter © 2007 Elsevier B.V. All rights reserved.
doi:10.1016/j.pepi.2007.05.009

ture (space group *Cmcm*) at *pT*-conditions corresponding to the D″-zone (e.g. Murakami et al., 2004, 2005; Hirose et al., 2005; Mao et al., 2004) has important implications for the core to mantle heat flux and deep Earth dynamics. The physiochemical properties of coexisting perovskite and post-perovskite and the Clapeyron slope of the phase transition are critical parameters in geodynamical models. The transition from perovskite to post-perovskite is associated with a large decrease in entropy combined with a small decrease in volume, resulting in a large positive Clayperon slope. The d*p*/d*T*-slope of the phase boundary in $MgSiO_3$ cannot be determined accurately in laser-heated diamond anvil cell experiments. Experiments using suitable analogue compounds where the pv–ppv-transition can be studied within the pressure ranges of the piston cylinder or multianvil apparatus may therefore be useful.

At atmospheric pressure the stable form of $CaIrO_3$ is the orthorombic post-perovskite (*Cmcm*), whereas the orthorombic perovskite (*Pbnm*) may form metastably (McDaniel and Schneidler, 1972). The latter phase is stable at high temperatures at somewhat higher pressures. Hirose and Fujita (2005) and Trønnes et al. (2006) investigated the pv–ppv-transition for $CaIrO_3$ at 1–3 GPa and 1350–1550 °C, and found d*p*/d*T*-slopes of about 16 and 24 MPa K^{-1}, respectively. In a calorimetric study of the $CaIrO_3$ polymorphs, Kojitani et al. (2007) determined an even larger transition slope of about 40 MPa K^{-1}. These slopes are considerably larger that those estimated for $MgSiO_3$ from first principles and *ab initio* models (Iitaka et al., 2004; Oganov and Ono, 2004) and from modelling of the topography of the upper and lower D″-discontinuities (Sidorin et al., 1999; Nakagawa and Tackley, 2004; Hernlund et al., 2004) assuming that these discontinuities are caused by the pv–ppv-transition. Clapeyron slopes ranging from 6 to 10 MPa K^{-1} have been used in such geodynamic modelling. Based on an ambient pressure thermal expansion study of ppv-$CaIrO_3$, Lindsay-Scott et al. (2007) found considerably larger elastic anisotropy in $CaIrO_3$ compared to $MgSiO_3$. This led them to conclude that the physical properties at atmospheric pressure make ppv-$CaIrO_3$ a very imperfect analogue for ppv-$MgSiO_3$. At slightly elevated pressures, however, this discrepancy may become smaller.

The pv–ppv-transition in $MgSiO_3$ is unusual in that the bulk and shear moduli may change in opposite directions across the phase boundary. Several seismic discontinuities that have been observed within the D″-zone show large lateral depth-variation and complexity (e.g. Lay et al., 2006). An uppermost discontinuity characterized by a shear wave velocity drop may be caused by a density jump due to compositional changes. The pv–ppv-transition seems to be related to a considerable shear wave speed increase. A locally developed and generally weaker shear wave decrease closer to the core–mantle boundary can be ascribed to the reverse transition from ppv to pv caused by the large thermal gradient near the core. As pointed out by Wookey et al. (2005) based on *ab initio* DFT calculations of elastic constants, the pv- to ppv-transition in $MgSiO_3$ is expected to cause discontinuities involving increasing shear wave velocity, v_s, decreasing bulk sound velocity, v_ϕ, and possibly slightly decreasing or constant pressure-wave velocity, v_p. These changes are caused by a small increase in density combined with higher shear modulus and lower bulk modulus in ppv relative to pv. The bulk modulus decrease from pv to ppv has been confirmed by experiments (Ono et al., 2006; Shieh et al., 2006).

Although the $CaIrO_3$ and $MgSiO_3$ are chemically very different, the fact that pv (*Pbnm*) and ppv (*Cmcm*) have identical space groups in both compounds makes the $CaIrO_3$-system an interesting study object, e.g. by experiments in the pressure and temperature range of 1–3 GPa and 1400–1550 °C. Several studies of experimental phase equilibria, single-crystal XRD characterization of bulk modulus and thermal expansivity, calorimetry and deformation mechanisms based on samples synthesized in this *p*,*T*-range are in progress or have recently been published. Here we present a density functional theory study of perovskite and post-perovskite $CaIrO_3$ with focus on the thermochemistry and thermophysics of the two polymorphs. Total energy calculations are used to derive the enthalpies, volumes and bulk moduli. The vibrational properties of the ground state structures are subsequently derived in the harmonic approximation using the direct method and the entropy of pv- and ppv-$CaIrO_3$ estimated from the vibrational densities of state.

The derived Clapeyron-slope of the ppv- to pv-transition may provide useful supplementary information on the geodynamics of D″ region. The complex seismicity of the lowermost mantle (e.g. Hernlund et al., 2004; Lay et al., 2006; Wookey et al., 2005), including the significant seismic anisotropy, is discussed in light of the calculated elastic constants and bulk and shear moduli.

2. Computational details

2.1. Structure of post-perovskite and perovskite $CaIrO_3$

Both structures are described in literature. However, while a detailed structural description is found for the

post-perovskite (Rodi and Babel, 1965), only lattice vectors are reported for pv-$CaIrO_3$ (Hirose and Fujita, 2005). For the post-perovskite, the standard *Cmcm* setting of space groups 63 is used in the present study. Ca occupies a *4c* site with fractional coordinates (0, *y*, 1/4), Ir a *4a* site (0, 0, 0), and O both a *4c* (0, *y*, 1/4) and a *8f* (0, *y*, *z*) site. For the perovskite, the non-standard *Pbnm* setting of space group 62 is used since this has been used widely in previous studies of pv- to ppv-transitions. Ca occupies a *4c* site with fractional coordinates (*x*, *y*, 1/4), Ir a *4b* site (1/2, 0, 0) and O both a *4c* (*x*, *y*, 1/4) and a *8d* (*x*, *y*, *z*) site. Polyhedron representations of the crystal structures are given in Fig. 1. While, pv-$CaIrO_3$ forms a three-dimensional structure based on corner-sharing octahedra only, ppv-$CaIrO_3$ contains a mixture of corner- and edge-sharing octahedra resulting in a layered structure. While the octahedra share corners along the *c*-axis, they share edges along the *a*-axis and the two-dimentional slabs are thus stacked along the *b*-axis.

No experimental information on the magnetic structures has to our knowledge been reported.

2.2. Structural optimization by total energy calculations

Structural optimizations with respect to all unit cell dimensions and atomic coordinates of both structures were performed using density functional theory within the generalized gradient approximation, using the PBE functional (Perdew et al., 1996) for the exchange-correlation contribution to the total energy. A sufficiently large basis of projected augmented plane waves was used as implemented in the Vienna *ab initio* simulation program (VASP) (Kresse and Hafner, 1993; Kresse and Furthmüller, 1999). Both polymorphs are here represented by periodic unit cells containing four formula units. The post-perovskite structure can alternatively be represented by a two formula unit primitive cell. To ensure high accuracy, the *k*-point density and the plane wave cutoff energy were increased until convergence. The cutoff energy for the plane wave basis was 700 eV, while the *k*-point densities were $9 \times 5 \times 5$ for *Cmcm* and $5 \times 5 \times 5$ for *Pbnm*. The chosen parameters give approximately the same *k*-point density in the reciprocal space. The Monkhorst-Pack mesh was used for both cells. All calculations correspond to $T = 0$ K and $P = 0$ bar. The calculated lattice vectors are compared with experimental values in Table 1.

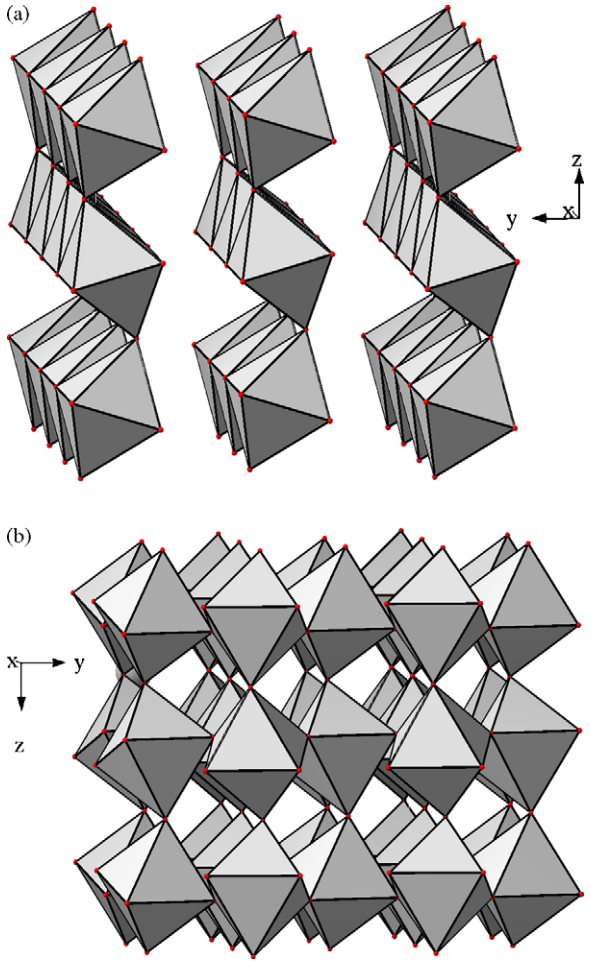

Fig. 1. Polyhedron representations of the post-perovskite (*Cmcm*) (upper) and the perovskite (*Pnma*) (lower) $CaIrO_3$ crystal structures.

The magnetic moment of iridium in ferromagnetic pv and ppv were calculated since the spin-state is impor-

Table 1
Lattice vectors for post-perovskite (*Cmcm*) and perovskite (*Pbnm*) $CaIrO_3$ at 1 bar and 0 K

Phase	*a* (Å)	*b* (Å)	*c* (Å)	*V* (Å^3)	Reference
ppv	3.2217	9.8487	7.3502	233.22	This work
ppv	3.144	9.865	7.297	226.32	Hirose and Fujita (2005)
ppv	3.14_5	9.85_5	7.29_3	226.04	Rodi and Babel (1965)
pv	5.3593	5.6905	7.7341	235.87	This work
pv	5.349	5.592	7.679	229.69	Hirose and Fujita (2005)

tant for the entropy of the transition. Iridium was in both structures found to be in the low-spin state. All other calculations were performed on non-spin polarized (NSP) systems. This is in part due to the computational cost and in part due to the lack of experimental information on the magnetic ordering. This simplification is not believed to affect the results significantly. Experimental studies of magnetic order–disorder transitions for inorganic compounds generally suggest that the difference in order–disorder enthalpies between two structures of a compound is small and that the effect of magnetic order on the lattice heat capacity is negligible.

2.3. Calculation of bulk modulus and its pressure derivative from E(V)

The bulk modulus, K_0, and its pressure derivative K_0' can be deduced from the variation of the total energy with volume. In the present study, both the Murnaghan and the Birch–Murnaghan equations of state were used (Andreson, 1995). The bulk modulus values were derived by calculating the total energy at different volumes, allowing all atomic positions and all lattice vectors to vary while keeping the volume fixed. The variation of the lattice vectors and volume with pressure were subsequently deduced using the Birch–Murnaghan equation of state to determine the pressure corresponding to a given volume. The bulk moduli for pv and ppv were also calculated imposing a constant K_0' of 4.0.

2.4. Calculation of elastic constants

The bulk modulus and the shear modulus can alternatively be determined from the elastic constants which determine the stiffness of the crystal against externally applied stresses. The elastic constants are presently determined by applying small strains to the equilibrium unit cells. For small deformations we expect Hooke's law to be valid and thus a quadratic dependence of the total energy on the strain. This quadratic behavior is described by the elastic constants, C_{ijkl}, that are derived through a Taylor expansion of the total energy for the system $E(V,\varepsilon)$ with respect to the strain ε (Wallace, 1972):

$$E(V, \varepsilon_{mn}) = E(V_0, 0) + V_0 \left(\sum_{ij} \sigma_{ij}\varepsilon_{ij} + \frac{1}{2}\sum_{ijkl} C_{ijkl}\varepsilon_{ij}\varepsilon_{kl} \right) + O(\varepsilon^3) \quad (1)$$

V_0 is the volume of the unstrained system with a corresponding energy $E(V_0,0)$. It is useful to use Voigt notation which takes advantage of the symmetries of the tensors: $xx \to 1, yy \to 2, zz \to 3, yz \to 4, xz \to 5, xy \to 6$. Using this notation, Eq. (4) becomes:

$$E(V, e_i) = E(V_0, 0) + V_0 \left(\sum_{i} \sigma_i e_i + \frac{1}{2}\sum_{ij} C_{ij} e_i e_j \right) + O(e^3) \quad (2)$$

with the strain tensor given by

$$\varepsilon = \begin{pmatrix} e_1 & \frac{1}{2}e_6 & \frac{1}{2}e_5 \\ \frac{1}{2}e_6 & e_2 & \frac{1}{2}e_4 \\ \frac{1}{2}e_5 & \frac{1}{2}e_4 & e_3 \end{pmatrix} \quad (3)$$

In order to calculate the nine elastic constants (C_{11}, C_{22}, C_{33}, C_{12}, C_{13}, C_{23}, C_{44}, C_{55} and C_{66}) of the orthorhombic structure, we apply nine independent strains to the lattice vectors. The parameterizations of the nine strains used here are given in Table 2. Variable-volume distortions are used since all calculations are performed at zero pressure. For each of the strains, the total energy was calculated for five to seven distortions, γ. The zero-, first- and second-order coefficients were found through polynomial fits. By solving the nine linearly independent equations, the nine elastic constants

Table 2
Parameterization of the nine strains used to calculate the nine elastic constant of the two orthorhombic structures

Strain I	Parameters (unlisted $e_i = 0$)	$\Delta E/V$ to $O(\gamma^2)$
1	$e_1 = \gamma$	$1/2\ C_{11}\gamma^2$
2	$e_2 = \gamma$	$1/2\ C_{22}\gamma^2$
3	$e_3 = \gamma$	$1/2\ C_{33}\gamma^2$
4	$e_1 = 2\gamma, e_2 = -\gamma, e_3 = -\gamma$	$1/2\ (4C_{11} - 4C_{12} - 4C_{13} + C_{22} + 2C_{23} + C_{33})\gamma^2$
5	$e_1 = -\gamma, e_2 = 2\gamma, e_3 = -\gamma$	$1/2\ (C_{11} - 4C_{12} - 2C_{13} + 4C_{22} - 4C_{23} + C_{33})\gamma^2$
6	$e_1 = -\gamma, e_2 = -\gamma, e_3 = 2\gamma$	$1/2\ (C_{11} + 2C_{12} - 4C_{13} + C_{22} - 4C_{23} + 4C_{33})\gamma^2$
7	$e_4 = \gamma$	$1/2\ C_{44}\gamma^2$
8	$e_5 = \gamma$	$1/2\ C_{55}\gamma^2$
9	$e_6 = \gamma$	$1/2\ C_{66}\gamma^2$

The energy expression is given by Eq. (2).

are found. The fractional coordinates were relaxed during all calculations.

2.5. Calculation of phonon dispersion relation

The phonon dispersion relations were calculated by the direct method using the PHONON software (Parlinski, 1999; Parlinski et al., 1997). Supercells were used in order to obtain accurate frequencies at several high symmetry points of the reciprocal lattice. For ppv-$CaIrO_3$ a 120 atoms $3 \times 1 \times 2$ super cell was sampled with a $2 \times 2 \times 2$ k-point mesh. A 80 atom $2 \times 1 \times 2$ super cell was sampled with a $2 \times 3 \times 2$ k-point mesh for pv-$CaIrO_3$. The atoms at unique lattice sites were displaced one at a time by 0.03 Å along the x, y and z-directions of the unit cell and the resulting Hellmann–Feynman forces calculated. To diminish systematical errors both positive and negative displacements were made about the equilibrium positions. Twenty-four independent displacements were made for both structures. The splitting of optical modes to transverse (TO) and longitudinal (LO) components is neglected.

3. Results

3.1. Structure, energetics and compressibility

The ground state properties of ppv-$CaIrO_3$ and pv-$CaIrO_3$ were derived by relaxing both the lattice vectors and all fractional coordinates. ppv-$CaIrO_3$ is found to be the lower-energy structure and thus the low-temperature modification in agreement with experiments. The calculated fractional coordinates for the different ions for ppv-$CaIrO_3$ and pv-$CaIrO_3$ are given in Table 3. In case of ppv-$CaIrO_3$ experimental values (Rodi and Babel, 1965) are also included in the table. The calculated structural parameters given in Tables 1 and 3 are in good agreement with the experimental values. In general, GGA overestimates equilibrium volumes, and agreement with experiment within 2% is considered good. The energy difference between the two modifications was calculated to be 11.8 kJ mol^{-1}. This is somewhat lower than the recently reported calorimetric value 32.2 ± 15.5 kJ mol^{-1} (Kojitani et al., 2007).

The bulk moduli and their pressure derivatives are deduced (using the Murnaghan and Birch–Murnaghan equations of state) from the variation of the total energy of the two structures with volume as given in Fig. 2. Only data points within $0.90 < V/V_0 < 1.10$ were used in the analyses. The bulk moduli obtained using the two different equations of state agree within 0.5%, giving $K_0 = 164$ and 178 GPa for ppv and pv, respectively (Table 4). The bulk modulus of ppv-$CaIrO_3$ at ambient pressure is about 9% lower than that for pv-$CaIrO_3$. A pressure derivative, K_0' of 3.9–4.0 for ppv-$CaIrO_3$ compared to 2.8–3.3 for pv-$CaIrO_3$ suggests that the difference in bulk modulus decreases with increasing pressure. High-pressure experiments and computations on $MgSiO_3$-system have yielded similar, but smaller magnitude, K_0'-differences between pv (3.9–4.1) (Oganov and Ono, 2004; Fiquet et al., 2000) and ppv (4.2–4.5) (Oganov and Ono, 2004; Tsuchiya et al., 2005; Tsuchiya et al., 2004). Because the difference in the pressure derivatives of the bulk modulus for pv and ppv is larger in our study compared with the results from pv and ppv in the $MgSiO_3$-system (e.g. Oganov and Ono, 2004; Fiquet et al., 2000), we also

Table 3
Fractional coordinates for post-perovskite (*Cmcm*) and perovskite (*Pbnm*) $CaIrO_3$ at 1 bar and 0 K

			This work	Rodi and Babel (1965)
ppv-$CaIrO_3$				
Ca	*4c*	*y*	0.250	0.2498
O	*4c*	*y*	0.924	0.933
O	*8f*	*y*	0.626	0.630
O	*8f*	*z*	0.452	0.445

			This work
pv-$CaIrO_3$			
Ca	*4c*	*x*	0.978
Ca	*4c*	*y*	0.064
O	*4c*	*x*	0.106
O	*4c*	*y*	0.458
O	*8d*	*x*	0.687
O	*8d*	*y*	0.303
O	*8d*	*z*	0.054

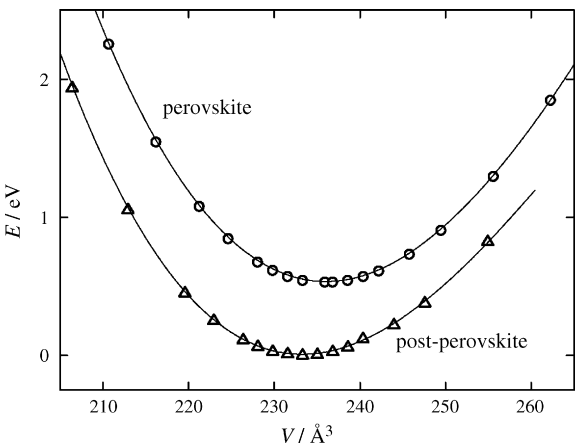

Fig. 2. E vs. V for perovskite (*Pnma*) and for post-perovskite (*Cmcm*) $CaIrO_3$ ($p = 1$ bar and $T = 0$ K).

Table 4
Calculated mechanical properties for post-perovskite (*Cmcm*) and perovskite (*Pbnm*) $CaIrO_3$ at 1 bar and 0 K

	Method	ppv	pv
K_0 (GPa)	Murnaghan	164.0	178.5
K_0'	Murnaghan	3.9	2.8
K_0 (GPa)	Murnaghan (K_0' fixed to 4)	165.6	171.7
K_0 (GPa)	Birch–Murnaghan	164.3	177.7
K_0'	Birch–Murnaghan	4.0	3.3
K_0 (GPa)	Birch–Murnaghan (K_0' fixed to 4)	164.1	172.4
K_0 (GPa)	Elastic constants—Voigt approximation	160.0	174.0
K_0 (GPa)	Elastic constants—Reuss approximation	153.4	168.7
G (GPa)	Elastic constants—Voigt approximation	73.8	60.6
G (GPa)	Elastic constants—Reuss approximation	64.2	56.7
E' (GPa)	Elastic constants	180.5	158.1
ν	Elastic constants	0.31	0.35

calculated the bulk modulus with a fixed value for K_0'. The effect on the calculated bulk modulus of keeping the K_0'-value fixed at 4.0 is, as expected, very small for ppv (with independently calculated K_0' of 3.9–4.0). For pv, however, this reduces the bulk modulus from about 178 to 172 GPa.

There is limited previous information about the compressibility of the $CaIrO_3$ polymorphs. The only experimental value we have found is a pressure derivative of the bulk modulus for ppv-$CaIrO_3$. The value, derived from thermal expansion data using a second-order Grüneisen approximation ($K_0' = 4.8 \pm 0.4$) (Lindsay-Scott et al., 2007), is somewhat higher than the value obtained here. Lindsay-Scott et al. (2007) also estimated the bulk modulus for ppv-$CaIrO_3$, assuming the Grüneisen parameter obtained in a DFT study of $MgSiO_3$ (Tsuchiya et al., 2004) to hold also for $CaIrO_3$. The resulting K_0 of 144 GPa is somewhat lower than the presently derived value.

The variation of the lattice vectors and volume with pressure are deduced from the Birch–Murnaghan equation of state using the obtained bulk moduli and their pressure derivatives. The changes in unit cell volumes (V/V_0) and individual crystallographic dimensions (a/a_0, b/b_0, c/c_0) as a function of pressure for ppv- and pv-$CaIrO_3$ are shown in Figs. 3 and 4. Both crystal structures are compressed in an aniosotropic

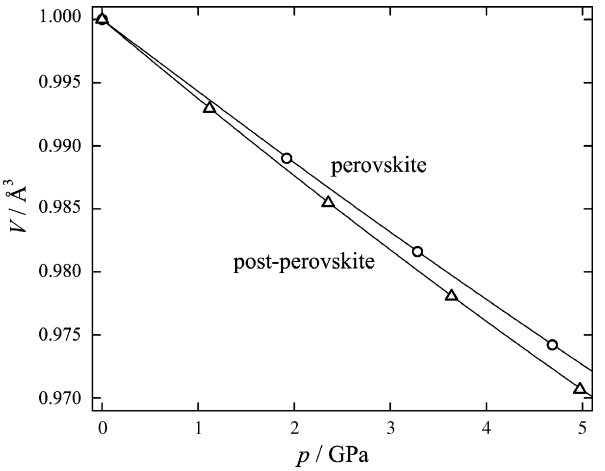

Fig. 3. V vs. p for perovskite (*Pnma*) and for post-perovskite (*Cmcm*) $CaIrO_3$ ($T = 0$ K, p derived from equation of state).

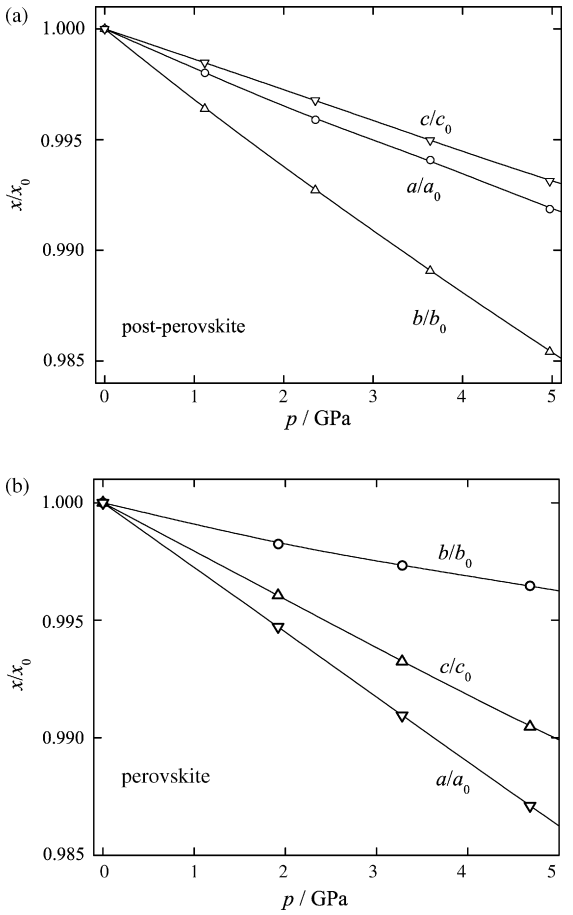

Fig. 4. (a) Lattice vectors vs. p for post-perovskite (*Cmcm*) $CaIrO_3$ ($T = 0$ K, p derived from equation of state), (b) Lattice vectors vs. p for perovskite (*Pnma*) $CaIrO_3$ ($T = 0$ K, p derived from equation of state).

fashion. For ppv-$CaIrO_3$ (Fig. 4a) the *a*- and *c*-axes are as expected less compressible than the *b*-axis which is perpendicular to the two-dimensional *ac*-layers.

$$K_0(V)=\frac{1}{9}(C_{11}+C_{22}+C_{33})+\frac{2}{9}(C_{12}+C_{13}+C_{23}) \quad (5)$$

$$G(R)=\frac{15}{4(S_{11}+S_{22}+S_{33})-4(S_{12}+S_{13}+S_{23})+3(S_{44}+S_{55}+S_{66})} \quad (6)$$

3.2. Elastic constants and derived mechanical properties

The elastic constants derived from the nine parameterizations of strains given in Table 2 are listed in Table 5. The constants obtained for pv- and ppv-$CaIrO_3$ satisfy all conditions required for mechanical stability (Wallace, 1972). The ppv-$CaIrO_3$ constants are clearly influenced by the layered structure resulting from edge-sharing of octahedra along the *a*-axis. This is reflected by high C_{11} and C_{33}, compared to C_{22} and low C_{12} and C_{13} compared to C_{23} (C_{22} is 61% of the average of C_{11} and C_{33} and the average of C_{12} and C_{13} is 64% of C_{23}). In contrast, the elastic constants for pv-$CaIrO_3$ are relatively similar, with C_{11}, C_{33} and C_{22} all within 21% of each other.

Polycrystalline bulk modulus and shear modulus are calculated from the elastic constants assuming a crystalline aggregate of randomly orientated single phase monocrystals. The determination of the stress or strain distribution in the aggregate with respect to external load can be derived for two extreme cases, uniform stress and uniform strain (Green, 1998). These approximations are termed the Reuss and Voigt approximations, respectively, and represent the upper and lower bounds for the elastic moduli of polycrystalline samples.

$$K_0(R)=\frac{1}{(S_{11}+S_{22}+S_{33})+2(S_{12}+S_{13}+S_{23})} \quad (4)$$

Table 5
Calculated elastic constants for post-perovskite (*Cmcm*) and perovskite (*Pbnm*) $CaIrO_3$ at 1 bar and 0 K

	ppv	pv
C_{11}	325.9	224.2
C_{22}	206.7	284.0
C_{33}	354.9	262.8
C_{12}	85.5	159.7
C_{13}	69.2	103.6
C_{23}	121.7	134.2
C_{44}	58.6	70.4
C_{55}	45.9	41.3
C_{66}	61.2	66.6

$$G(V)=\frac{1}{15}(C_{11}+C_{22}+C_{33}-C_{12}-C_{13}-C_{23})+\frac{1}{5}(C_{44}+C_{55}+C_{66}) \quad (7)$$

Here C_{ij} are the elastic constants while S_{ij} are the corresponding compliance constants. Estimates of the Poisson's ratio, ν, and the Young's modulus, E', are obtained by substituting the average values of K_0 and G in:

$$\nu=\frac{1}{2}\left(1-\frac{3G}{3K_0+G}\right) \quad (8)$$

and

$$E'=\left(\frac{1}{3G}+\frac{1}{9K_0}\right)^{-1} \quad (9)$$

Values of the bulk and shear moduli, Poissons ratio and Youngs modulus are given in Table 4. In agreement with the results from the Birch–Murnaghan equation of state, the bulk modulus of ppv-$CaIrO_3$ is about 14 GPa (9%) lower than that of pv-$CaIrO_3$. In contrast, the shear modulus of ppv is about 10 GPa (15%) higher than that of pv.

The elastic anisotropy is characterized by the differences between the linear bulk moduli as well as the shear anisotropic factors. The bulk moduli along the *a*, *b* and *c*-axes can be calculated from the presently obtained compliance factors (Nye, 1957) as

$$K_a=\frac{1}{(S_{11}+S_{12}+S_{13})} \quad (10)$$

$$K_b=\frac{1}{(S_{12}+S_{22}+S_{23})} \quad (11)$$

$$K_c=\frac{1}{(S_{13}+S_{23}+S_{33})} \quad (12)$$

The derived values, listed in Table 6, are in very good agreement with the variation of the lattice vectors with pressure (Fig. 4) deduced from the Birch–Murnaghan equation-of-state analysis.

The shear anisotropic factors are (Ravindran et al., 1998):

$$A_1=\frac{4C_{44}}{(C_{11}+C_{33}-2C_{13})} \quad (13)$$

Table 6
Linear bulk moduli (in GPa) and shear anisotropy factors defined by Eqs. (13)–(15)

	$CaIrO_3$		$MgSiO_3$		Al_2O_3	
	ppv	pv	ppv	pv	ppv	Pv
K_a	517	359	1894	1422	2294	1761
K_b	307	1122	1362	2294	2037	3205
K_c	755	444	2058	1822	2110	1721
K_b/K_a	0.59	3.12	0.72	1.61	0.89	1.82
K_c/K_a	1.46	1.24	1.09	1.28	0.92	0.98
A_1	0.43	1.01	0.72	1.19	0.64	1.07
A_2	0.58	0.59	0.92	0.89	0.55	0.80
A_3	0.68	1.49	1.06	1.27	1.04	0.98

Data for $MgSiO_3$ (117 GPa, 2300 K) and Al_2O_3 (136 GPa, 0 K) are taken from Wookey et al. (2005) and Stackhouse et al. (2005a,b).

For the $\{1\,0\,0\}$ shear planes in $\langle 0\,1\,0\rangle$ and $\langle 0\,1\,1\rangle$ directions:

$$A_2 = \frac{4C_{55}}{(C_{22} + C_{33} - 2C_{23})} \tag{14}$$

For the $\{0\,1\,0\}$ shear planes in $\langle 0\,0\,1\rangle$ and $\langle 1\,0\,1\rangle$ directions:

$$A_3 = \frac{4C_{66}}{(C_{11} + C_{22} - 2C_{12})} \tag{15}$$

For the $\{0\,0\,1\}$ shear planes in $\langle 1\,0\,0\rangle$ and $\langle 1\,1\,0\rangle$ directions. The shear anisotropy factors are also given in Table 6. The deviation of the anisotropy factors from unity is a measure for the elastic anisotropy.

3.3. Lattice dynamics and vibrational properties

The calculated phonon dispersion relations for ppv- and pv-$CaIrO_3$ are shown in Fig. 5a and b. At the high symmetry points of the lattice a large degree of degeneration is seen. The perovskite and post-perovskite phases contain 4 and 2 formula units per primitive unit cell, respectively. According to group theory, the $57+3$ phonon modes at Γ-point for the perovskite structure decompose as irreducible representation: $7A_g + 5B_{1g} + 7B_{2g} + 5B_{3g} + 8A_u + 10B_{1u} + 8B_{2u} + 10B_{3u}$. Similarly for the post-perovskite, the $27+3$ phonon modes at the Γ-point decompose as $4A_g + 3B_{1g} + 1B_{2g} + 4B_{3g} + 2A_u + 6B_{1u} + 6B_{2u} + 4B_{3u}$. For both structures, all g modes are Raman active, while all u modes expect the A_u ones are IR active. Further details will be published separately.

The normalized phonon densities of states, $g(\omega)$, for the supercells shown in Fig. 6 are found by integration. A simple harmonic approximation is used to calculate the molar heat capacity from these phonon densities of states, $g(\omega)$. The heat capacity is per formula unit:

$$C_V = nk_B \int_0^\infty \left(\frac{\hbar\omega}{kT}\right) \frac{e^{\hbar\omega/k_BT}}{(e^{\hbar\omega/k_BT} - 1)^2} g(\omega)\,d\omega \tag{16}$$

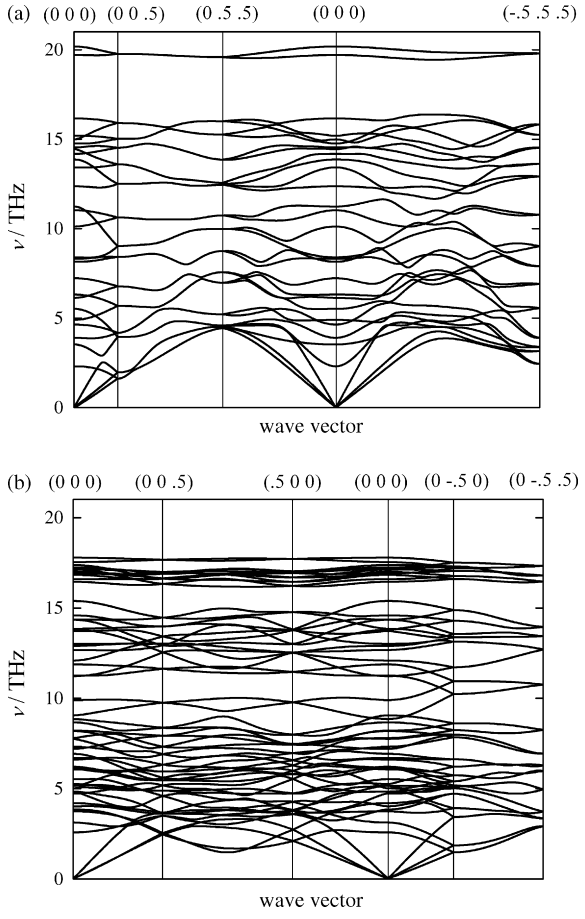

Fig. 5. (a) Dispersion relation for post-perovskite (*Cmcm*) $CaIrO_3$ ($p = 1$ bar and $T = 0$ K). (b) Dispersion relation for perovskite (*Pnma*) $CaIrO_3$ ($p = 1$ bar and $T = 0$ K).

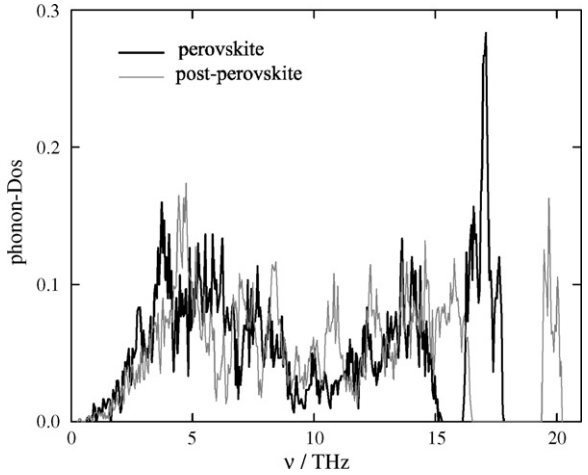

Fig. 6. Phonon density of state for perovskite (*Pnma*) and for post-perovskite (*Cmcm*) $CaIrO_3$ ($p = 1$ bar and $T = 0$ K).

where n is the number of atoms, $\hbar$ the Planck constant and k_B is the Boltzmann constant. The calculated molar heat capacities and the derived molar entropies are given in Figs. 7 and 8, respectively. At 298 K the difference in entropy is $6.3\,J\,K^{-1}\,mol^{-1}$. Above 298 K the heat capacities of the two phases are very similar and the entropy difference increases only by $0.4\,J\,K^{-1}\,mol^{-1}$ between 298 and 1500 K. A main question is to what extent these entropies converge with regards to cell-size. We have addressed that question by calculating the thermodynamic parameters also for the $1 \times 1 \times 1$ unit cells which give exact vibrational frequencies only at the Brillouin zone center (the Γ-point). The molar entropy at 298 K increases from 103.0 to $105.5\,J\,K^{-1}\,mol^{-1}$ going from a $1 \times 1 \times 1$ unit cell to a $2 \times 1 \times 2$ super cell for pv-$CaIrO_3$. For ppv-$CaIrO_3$,

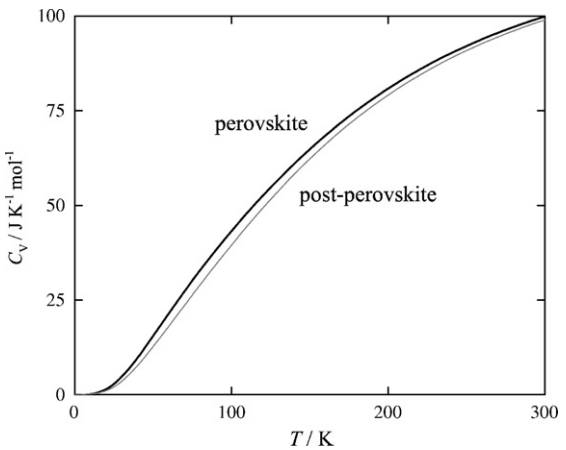

Fig. 7. Molar heat capacity for perovskite (*Pnma*) and for post-perovskite (*Cmcm*) $CaIrO_3$ at 1 bar.

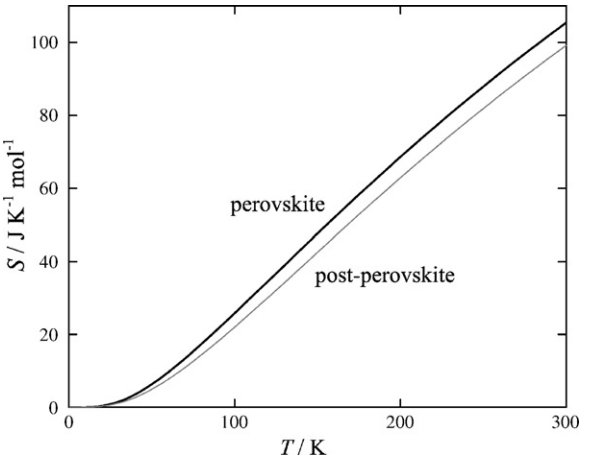

Fig. 8. Molar entropy for perovskite (*Pnma*) and for post-perovskite (*Cmcm*) $CaIrO_3$ at 1 bar.

the molar entropy decreases from $99.8\,J\,K^{-1}\,mol^{-1}$ for a $1 \times 1 \times 1$ unit cell to $99.2\,J\,K^{-1}\,mol^{-1}$ for a $3 \times 1 \times 2$ super cell. The entropy difference thus increased from 3.2 to $6.3\,J\,K^{-1}\,mol^{-1}$ at 298 K. The change in entropy is expected to be small when increasing the size of the super cell further. This expectation, however, cannot be tested due to the prohibitive cost involved.

3.4. High pressure behaviour

Based on the calculations presented above we can estimate the slope of the ppv–pv phase boundary. The Clapeyron equation may be written as

$$\frac{dp}{dT} = \frac{\Delta S}{\Delta V} = \frac{\Delta H}{T_{trs}\Delta V} \tag{17}$$

We are not able to produce a pure *ab initio* value of the slope since we are not able to calculate all contributions to the entropy of transition. However, we can calculate a slope based on the calculated enthalpy of transition ($11.8\,kJ\,mol^{-1}$) and the calculated volume of transition ($0.64\,Å^3$ pr formula unit or $0.40\,cm^3\,mol^{-1}$). By assuming an extrapolated experimental value for a hypothetical transition temperature at ambient pressure of 1380 °C (1673 K), we obtain a dp/dT-slope of $18\,MPa\,K^{-1}$. The resulting phase boundary is compared with literature values in Fig. 9. It is difficult to estimate the accuracy of this value and it should be noticed that the calculated and experimental volumes of transition varies between 0.32 and $0.51\,cm^3\,mol^{-1}$ (Hirose and Fujita, 2005; Trønnes et al., 2006). This dp/dT-slope is intermediate between the experimentally determined slopes of about $16\,MPa\,K^{-1}$ (Hirose and Fujita, 2005) and $24\,MPa\,K^{-1}$ (Trønnes et al., 2006). In a solution calorimetric study Kojitani et al.

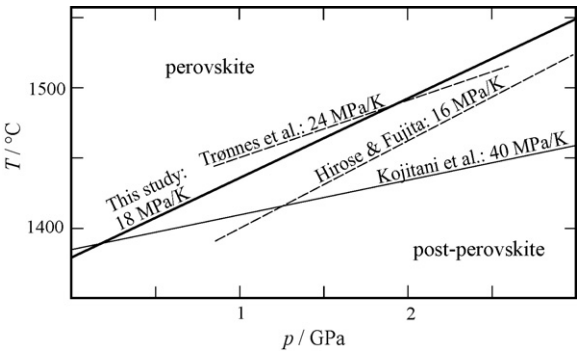

Fig. 9. Compilation of pv–ppv phase boundaries for $CaIrO_3$ from various studies. Phase equilibria from quenching experiments: Hirose and Fujita (2005) and Trønnes et al. (2006); from calorimetry: Kojitani et al. (2007); from DFT-modeling: this study.

(2007) obtained a very large, and rather uncertain slope of $40 \pm 19\,MPa\,K^{-1}$, with the quoted uncertainty based on the standard deviations reported for their enthalpy change.

4. Discussion

Our computationally derived enthalpy difference between the two $CaIrO_3$ polymorphs is small compared to the only experimental value (Kojitani et al., 2007), and further experimental and computational studies are needed to accurately resolve this issue. The solution calorimetric determination of the enthalpy difference between pv and ppv-$CaIrO_3$ (Kojitani et al., 2007) suggest that the entropy of ppv is as much as $19.4 \pm 9.3\,J\,K^{-1}\,mol^{-1}$ lower than for pv. Kojitani et al. (2007) suggest the difference in structural connectivity as the origin of the entropy difference. Whereas pv-$CaIrO_3$ consists of corner-sharing octahedra only, the ppv-structure contains edge-sharing octahedra along the *a*-axis. The more rigid edge-linking may restrict some phonons, in particular those involving rotational motion of the octahedra (Kojitani et al., 2007). Although we in principle agree with this line of reasoning, the magnitude of this effect is probably insufficient to account for the large entropy difference obtained by (Kojitani et al., 2007). In a recent study of $SrMnO_3$ (Søndenå et al., 2007) we determined, both experimentally and computationally, the heat capacity and entropy of two polymorphs differing even more in connectivity. Whereas cubic $SrMnO_3$ has corner-sharing octahedra only, the hexagonal polymorph contains 50% corner-sharing and 50% face-sharing octahedra. In this case the entropy change at 298 K is as small as $5.5\,J\,K^{-1}\,mol^{-1}$ (Søndenå et al., 2007). We do not expect the difference in the dilational contribution to the heat capacity, and thus to the entropy, to be large enough to explain the difference between the entropy change based on the solution calorimetry (Kojitani et al., 2007) and that obtained here. On the other hand, it is clear that electronic contributions to the heat capacity and thus the entropy are significant if ppv- or pv-$CaIrO_3$ or both are metallic. Information on the electrical properties of $CaIrO_3$, however, are not available. Other ternary iridium oxides such as $BaIrO_3$ and Sr_2IrO_4 in which the Ir is in the formal Ir^{4+}-state are known to show weak ferromagnetism with a relatively high disordering temperature and to show unusual electrical properties with overall semiconducting behavior (Kini et al., 2006). It is important to note that both the pv and ppv modifications are low-spin at least in the ferromagnetic state. A difference in spin state between the two structures could have induced a significant entropy of transition. Thus, the entropy difference between pv and ppv appears to be smaller than that proposed by Kojitani et al. (2007). The standard deviation reported in that study, however, is very large.

The entropy difference between pv- and ppv-$CaIrO_3$ can also be estimated from the experimental determination of the Clapeyron slopes and the volume change of the transition (Hirose and Fujita, 2005; Trønnes et al., 2006). The values of $16\,MPa\,K^{-1}$ and $0.507\,cm^3\,mol^{-1}$ (Hirose and Fujita, 2005) and $24\,MPa\,K^{-1}$ and $0.321\,cm^3\,mol^{-1}$ (Trønnes et al., 2006) gives entropy differences between pv and ppv of 8.11 and $8.02\,J\,K^{-1}\,mol^{-1}$, respectively. These entropy changes are in reasonable agreement with the entropy difference estimated presently from the calculated phonon dispersion relations, $6.3\,J\,K^{-1}\,mol^{-1}$. In conclusion, the present study and the previously determined Clapeyron slopes give a consistent picture that indicate that the enthalpy and thus the entropy of the pv to ppv transition is overestimated in the recent calorimetric study (Kojitani et al., 2007).

The negative and positive changes in bulk and shear moduli, respectively, across the pv- to ppv-transition boundary is strongly linked to the nature of the crystal structure. Edge-sharing octahedra along the *a*-axis in the ppv-structure give rise to high values of C_{11} and C_{33}, i.e. high resistance towards stress in the *ac*-plane of the 2D slabs. For the same reason C_{12} and C_{13} are low for the ppv-structure. Whereas the bulk modulus (in the Voigt approximation) is related to the sum of $(C_{11} + C_{22} + C_{33})$ and $(C_{12} + C_{13} + C_{23})$, the shear modulus is related to their difference. The bulk and shear moduli changes across the transition is thus explained by the higher $(C_{11} + C_{22} + C_{33})$- and lower $(C_{12} + C_{13} + C_{23})$-sum of the ppv- compared to the pv-structure.

Table 6 presents a comparison of the elastic anisotropy of $CaIrO_3$, $MgSiO_3$ and Al_2O_3 based on this study, (Wookey et al., 2005) and (Stackhouse et al., 2005a,b), respectively. It should be noted that Oganov and Ono (2005) concluded that a Rh_2O_3(II)-structured phase of Al_2O_3 transforms directly to ppv-Al_2O_3 at about 120 GPa and 0–2500 K, without any intervening pv-stability field. They indicated, however, that there may be a pv-stability field at temperatures above 2500 K. With this caveat for Al_2O_3 in mind, it is interesting to note the close correspondence between the various linear bulk moduli and shear anisotropy factors of pv and ppv for the three different compositions. The similar elastic properties for the systems $CaIrO_3$, $MgSiO_3$ and Al_2O_3 seem promising in terms of using pv- and ppv-$CaIrO_3$ as low-pressure analogues for the corresponding deep Earth minerals in $(Mg,Fe^{2+})SiO_3$-dominated systems with minor, but significant Al_2O_3- and Fe_2O_3-components.

A comparison between the compressional and thermal anisotropy of ppv-$CaIrO_3$ can be based on our DFT-computational study and the experimental determination of thermal expansivity by Lindsay-Scott et al. (2007). These results indicate that the pressure-induced elastic anisotropy is considerably larger than the thermal anisotropy. Whereas the *b*-axis has the greatest thermal expansion and isothermal compressibility, the least compressible *c*-axis does not correspond to the direction of the lowest thermal expansion, i.e. the *a*-axis (Lindsay-Scott et al., 2007). The strong elastic anisotropy of ppv, documented from DFT-computations of both $MgSiO_3$ and $CaIrO_3$ corresponds to the well-developed seismic anisotropy of D″-zone (Lay et al., 2006; Wookey et al., 2005).

The *Pbnm* perovskites of $CaIrO_3$ and $MgSiO_3$ have open and flexible crystal structures with corner-linked octahedra and high entropy. The phase transitions into and out of the perovskite stability field are therefore endothermic and exothermic, respectively. The moderately endothermic perovskite-forming reaction in $MgSiO_3$-dominated compositions associated with the 660 km seismic discontinuity has a negative dp/dT-slope of −2 to −3 MPa K^{-1} (Weidner and Wang, 2000), whereas the exothermic post-perovskite-forming transitions defining the main D″-discontinuity have a much larger and positive dp/dT-slope. The exothermic nature of the post-perovskite forming reaction is enhanced by the notably low entropy of post-perovskite, associated with a major structural reorganization and transition to 33% corner-linked octahedra. The 660 km discontinuity has a relatively simple seismological expression in the form of increasing v_p and v_s. The sharp discontinuity is followed by velocity gradients in the 660–720 km depth range associated with delayed transformation of majoritic garnet to more aluminous perovskite (Kennett et al., 1995; Shearer, 2000). The D″ discontinuities, however, are considerably more complicated. As indicated by Lay et al. (2006), the uppermost discontinuity, associated with a minor velocity decrease, may be caused by densification associated with compositional layering. The next deeper and major discontinuity, characterized by increasing v_s and largely unchanged or even slightly decreasing v_p, requires the unusual combination of increasing shear modulus and decreasing bulk modulus across the interphase. A lower and reverse discontinuity (decreasing v_s) within 50–100 km of the core–mantle boundary (Lay et al., 2006) may represent a transition where post-perovskite reverts to perovskite due to large thermal gradients near the outer core.

The shear and bulk moduli requirements for the two latter discontinuities are consistent with the DFT-computational results of Wookey et al. (2005) for $MgSiO_3$ and this study for the $CaIrO_3$-analogue composition. Other *ab initio* calculations at 100–120 GPa (Oganov and Ono, 2004; Iitaka et al., 2004) show slightly smaller increases of shear modulus across the $MgSiO_3$ pv to ppv phase transition (3–5% versus 6–8% in (Wookey et al., 2005)) and almost no change in the bulk modulus. High-pressure experimental bulk modulus determinations for $MgSiO_3$, however, show decreases across the pv–ppv transition of 10–20% (Shieh et al., 2006; Stackhouse et al., 2005a,b), largely consistent with our computational $CaIrO_3$-results.

The large Clayperon slope resulting from the small volume increase and large entropy decrease of the pv–ppv-transition has important geodynamic implications. The large topography of the discontinuity associated with lateral temperature variation near the core–mantle boundary will in principle promote convection and heat transfer in the D″-zone. However, this effect may be largely cancelled by pronounced compositional layering, involving intrinsically dense thermochemical piles enriched in subducted basaltic material or material with elevated Fe/Mg-ratio. The observations of Torsvik et al. (2006) may indicate that sub-Pacific and sub-African thermochemical piles above the core–mantle boundary have been intact and stable over more than 250 Ma.

5. Conclusions

Our *ab initio* computational study of the thermodynamics and elasticity of the pv- and ppv-phases in the system $CaIrO_3$ are broadly consistent with

experiments and published DFT-results on the $MgSiO_3$-composition. Therefore, the $CaIrO_3$ system may be a promising low-pressure analogue for the Al- and Fe-bearing $MgSiO_3$-dominated pv and ppv of the lowermost mantle. The results show that the pv–ppv transition in $CaIrO_3$ is associated with decreasing volume (about 1%) and entropy (about 20%), resulting in a large dp/dT-slope of 18 MPa K^{-1} for the phase boundary, broadly consistent with recent experimental phase equilibrium investigations.

The calculated elastic anisotropy of pv and ppv in Ca corresponds well with the relations derived for the $MgSiO_3$-polymorphs by similar studies. As expected, the b-axis of ppv (normal to the partly edge-linked octahedral networks of the ac-layers) is considerably more compressible than the a- and c-axes. In perovskite, the b-axis is the least compressible. The shear modulus increases by about 15% and the bulk modulus decreases by about 9% across the pv–ppv transition. This finding is consistent with DFT-results in the $MgSiO_3$ system and with seismic observation of anti-correlated v_s and v_ϕ across the main D″-discontinuity.

Acknowledgments

The Research Council of Norway (Programme for Supercomputing) has supported the work through a grant of computing time. This project is motivated by and complementary to an experimental study of the $CaIrO_3$ polymorphs funded in part by EU Research Infrastructure Transnational Access Programme (The Structure and Properties of Materials at High Pressure) at Bayerisches Geoinstitut. We thank John Brodholt and an anonymous reviewer for perceptive and helpful reviews and Dave Rubie for editorial handling.

References

Andreson, O.L., 1995. Equation of State for Solids for Geophysics and Ceramic Science. Oxford University Press.

Fiquet, G., Dewale, A., Andrault, D., Kunz, M., Le Bihan, T., 2000. Thermoelastic properties and crystal structure of $MgSiO_3$ perovskite at lower mantle pressure and temperature conditions. Geophys. Res. Lett. 27, 21–24.

Green, D.J., 1998. An Introduction to the Mechanical Properties of Ceramics. Cambridge University Press.

Hernlund, J.W., Thomas, C., Tackley, P.J., 2004. A doubling of the post-perovskite phase boundary and structure of the Earth's lowermost mantle. Nature 434, 882–886.

Hirose, K., Fujita, Y., 2005. Clapeyron slope of the post-perovskite phase transition in $CaIrO_3$. Geophys. Res. Lett. 32, L13313, doi:10.1029/2005GL023219.

Hirose, K., Takafuji, N., Sata, N., Ohishi, Y., 2005. Phase transition and density of subducted MORB crust in the lower mantle. Earth Planet. Sci. Lett. 237, 239–251.

Iitaka, T., Hirose, K., Kawamura, K., Murakami, M., 2004. The elasticity of the $MgSiO_3$ post-perovskite phase in the Earth's lowermost mantle. Nature 430, 442–445.

Kennett, B.L.N., Engdahl, E.R., Buland, R., 1995. Constraints on the velocity structure of the Earth from travel times. Geophys. J. Int. 122, 108–124.

Kini, N.S., Strydom, A.M., Jeevan, H.S., Geibel, C., Ramakrishnan, S., 2006. Transport and thermal properties of weakly ferromagnetic Sr_2IrO_4. J. Phys.: Condens. Matter 18, 8205–8216.

Kojitani, H., Furukawa, A., Akaogi, M., 2007. Thermochemistry and high-pressure equilibria of the post-perovskite phase transition in $CaIrO_3$. Am. Mineral. 92, 229–232.

Kresse, G., Furthmüller, J., 1999. Efficient iterative schemes for *ab initio* total-energy calculations using a plane-wave basis set. Phys. Rev. B 54, 11169–11186.

Kresse, G., Hafner, J., 1993. *Ab initio* molecular dynamics for liquid metals. Phys. Rev. B 47, 558–561.

Lay, T., Hernlund, J., Garnero, E., Thorne, M.S., 2006. A post-perovskite lens and D″ heath flux beneath the central Pacific. Science 314, 1272–1276.

Lindsay-Scott, A., Wood, I.G., Dobson, D.P., 2007. Thermal expansion of CaIrO3 determined by X-ray powder diffraction. Phys. Earth Planet. Int. 162, 140–148.

Mao, W.L., Shen, G., Prakapenka, V.B., Meng, Y., Cambell, A.J., Heinz, D., Shu, J., Hemley, R.J., Mao, H.K., 2004. Ferromagnesian postperovskite silicates in the D″ layer of the earth. Proc. Natl. Acad. Sci. USA 101, 15,867–15,869.

McDaniel, C.L., Schneidler, S.J., 1972. Phase relations in the CaO–IrO_2–Ir system in air. J. Solid State Chem. 4, 275–280.

Murakami, M., Hirose, K., Kawamura, K., Sata, N., Ohishi, Y., 2004. Post-perovskite phase transition in $MgSiO_3$. Science 304, 855–858.

Murakami, M., Hirose, K., Sata, N., Ohishi, Y., 2005. Post-perovskite phase transition and mineral chemistry in the pyrolitic lower mantle. Geophys. Res. Lett. 32, L03304, doi:10.1029/2004GL021956.

Nakagawa, T., Tackley, P.J., 2004. Effects of a perovskite-post perovskite phase change near core-mantle boundary in compressible mantle convection. Geophys. Res. Lett. 31, L16611, doi:10.1029/2004GL020648.

Nye, J.F., 1957. Physical Properties of Crystals. Clarendon Press, Oxford.

Oganov, A.R., Ono, S., 2004. Theoretical and experimental evidence for a post-perovskite phase of $MgSiO_3$ in Earth's D″ layer. Nature 430, 445–448.

Oganov, A.R., Ono, S., 2005. The high-pressure phase of alumina and implications for the Earth's D″ layer. Proc. Nat. Acad. Sci. 102, 10828–10831.

Ono, S., Kikegawa, T., Ohishi, Y., 2006. Equation of state of the $CaIrO_3$-type $MgSiO_3$ up to 144 GPa. Am. Mineral. 91, 475–478.

Parlinski, K., 1999. Calculation of phonon dispersion curves by the direct method, Amer. Inst. Phys., Conference Proceedings 476 "Neutrons and Numerical Methods N_2M", ed. M.R. Johnson, G.G. Kearley, H.G Buttner, p. 121.

Parlinski, K., Li, Z.Q., Kawazoe, Y., 1997. First-principles determination of the soft mode in cubic ZrO_2. Phys. Rev. Lett. 78, 4063–4066.

Perdew, J.P., Burke, K., Ernzerhof, M., 1996. Generalized gradient approximation made simple. Phys. Rev. Lett. 77, 3865–3868.

Ravindran, P., Fast, L., Korzhavyi, P.A., Johansson, B., Wills, J., Eriksson, O., 1998. Density functional theory for calculation of orthorhombic crystals; Application to $TiSi_2$. J. Appl. Phys. 84, 4891–4904.

Rodi, F., Babel, D., 1965. Ternare oxide der übergangsmetalle. 4. Erdalkaliiridium(4)-oxide—kristallstruktur von $CaIrO_3$. Z. Anorg. Allg. Chem. 336, 17–23.

Shearer, P.M., 2000. Upper mantle seismic discontinuities, in: S.-i. Karato et al. (eds.) Earth's Deep Interior, Mineral Physics and Tomography From the Atomic to the Global Scale. Am. Geophys. Union. Monograph 117, 115–131.

Shieh, S.R., Duffy, T.S., Kubo, A., Prakapenka, V.B., Sata, N., Hirose, K., Ohishi, Y., 2006. Equation of state of the postperovskite phase synthesized from a natural (Mg,Fe)SiO_3 orthopyroxene. Proc. Natl. Acad. Sci. 103, 3039–3043.

Sidorin, I., Gurnis, M., Helmberger, D.V., 1999. Evidence for a ubiquitous seismic discontinuity at the base of the mantle. Science 286, 1326–1329.

Søndenå, R., Stølen, S., Ravindran, P., Grande, T., 2007. Heat capacity and lattice dynamics of cubic and hexagonal SrMnO3: calorimetry and DFT simulations. Phys. Rev. B., in press.

Stackhouse, S., Brodholt, J.P., Price, G.D., 2005a. High temperature elastic anisotropy of the perovskite and post-perovskite polymorphs of Al_2O_3. Geophys. Res. Lett. 32, L13305.

Stackhouse, S., Brodholt, J.P., Wookey, J., Kendall, J.-M., Price, G.D., 2005b. The effect of temperature on the seismic anisotropy of the perovskite and post-perovskite polymorphs of $MgSiO_3$. Earth. Planet. Sci. Lett. 230, 1–10.

Torsvik, T.H., Smethhurst, M.A., Burke, K., Steinberger, B., 2006. Large igneous provinces generated from the margins of the large low-velocity provinces in the deep mantle. Geophys. J. Int., 1–14, doi:10.1111/j. 1365-246X.

Trønnes, R.G., Frost, D.J., Boffa-Ballaran, T., Stølen, S., 2006. The perovskite to post perovskite transition in $CaIrO_3$. American Geophysical Union Fall Meeting, MR11A97.

Tsuchiya, T., Tsuchiya, J., Umemoto, K., Wentzcovitch, R.M., 2004. Phase transition in $MgSiO_3$ perovskite in the earth's lower mantle. Earth. Planet. Sci. Lett. 224, 241–248.

Tsuchiya, J., Tsuchiya, J., Wentzcovitch, R.M., 2005. Vibrational and thermodynamic properties of $MgSiO_3$ postperovskite. J. Geophys. Res. 110, B02204.

Wallace, D.C., 1972. Thermodynamics of Crystals. Wiley, New York.

Weidner, D.J., Wang, Y., 2000. Phase transitions: implications for mantle structure, in: S.- i. Karato et al. (eds.) Earth's Deep Interior, Mineral Physics and Tomography From the Atomic to the Global Scale. Am. Geohys. Union, Monogr. 117, 215–235.

Wookey, J., Stackhouse, S., Kendall, J.M., Brodholt, J., Price, D., 2005. Efficacy of the post-perovskite phase as an explanation for the lowermost-mantle seismic properties. Nature 438, 1004–1007.